ACS APPLIED ENERGY MATERIALS

www.acsaem.org

Article

Computational Screening of 2D Transition Metal Halides for Optical Applications: The Role of Excitonic Effects

Natan M. Regis, Juarez L. F. Da Silva, and Matheus P. Lima*

Cite This: https://doi.org/10.1021/acsaem.5c00610

Read Online

ABSTRACT: Transition metal halides (TMHs) have recently emerged as a promising class of two-dimensional (2D) materials for optoelectronic applications. However, a deep atomistic understanding of excitonic effects, arising in TMHs from the interplay between quantum confinement and diminished dielectric screening, is required for the design of future technological applications. In this work, we investigate 2D TMHs by combining density functional theory atomistic simulations, tight-binding models, and the solution of the Bethe–Salpeter equation. The selected 2D TMHs were obtained from the computational 2D materials database (C2DB) based on specific criteria to identify compounds with promising potential for optoelectronic applications. Our calculated lattice parameters are in agreement with those reported in both the C2DB database and the literature. However, deviations in electronic properties are observed for a few systems due to particularities in the implementation of spin–orbit coupling and hybrid functionals. We also predict exciton binding energies ranging from 0.23 to 0.81 eV, with TiI_2 in the space group $P\bar{6}m2$ exhibiting unusual excitonic insulator behavior. Excitons significantly impact optical absorption by reducing the maximum absorption coefficient and shifting the absorption peak, all of which were quantified throughout the manuscript. Furthermore, when evaluating potential heterojunctions using Anderson's rule, we find that excitonic effects modify 90 out of 276 possible heterojunctions, decreasing the number of type II heterojunctions, which are particularly relevant for optoelectronic applications.

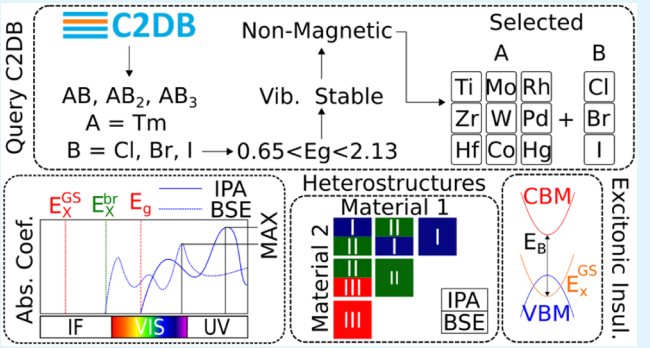

KEYWORDS: *transition metal halides, excitons, two-dimensional materials, excitonic insulator, density functional theory, tight-binding, Bethe–Salpeter equation*

1. INTRODUCTION

The research domain of two-dimensional (2D) materials has experienced significant advancements following the seminal work of Geim and Novoselov on graphene isolation, in which a single graphene monolayer was effectively separated from graphite using the Scotch tape exfoliation technique.[1] Over the years, numerous characterization techniques have showcased the unprecedented properties of graphene, such as high electrical and thermal conductivities, and exceptional mechanical properties,[2] however, it lacks an electronic band gap, which is a limiting factor for eventual optoelectronic applications. Thus, motivated by the successful isolation of graphene, researchers have turned their efforts to obtaining alternative 2D materials with semiconductor behavior, which show promise for a wide range of applications, including optoelectronics and microelectronics.

In this context, transition metal dichalcogenide (TMD) monolayers have emerged as strong candidates among other 2D materials due to their intriguing optoelectronic characteristics. For example, the 2H phase of TMDs such as MoS_2, $MoSe_2$, WS_2, and WSe_2 has attracted significant interest for its easy synthesis and remarkable optical properties.[3] Specifically, TMDs based on tungsten (W) and molybdenum (Mo) are the most investigated and exhibit notable photoluminescence (PL) effects, the intensity of PL being dependent on the number of layers.[4] Moreover, TMDs have demonstrated potential for various optoelectronics applications, including transistors, memory devices, valleytronics, and photovoltaics.[5−7] It is worth noting that some monolayers of TMDs exhibit PL orders of magnitude stronger than their bulk counterparts,[4] demonstrating the peculiar optical properties of 2D materials.

The distinct optoelectronic properties of two-dimensional materials can be ascribed to excitons, which are electron–hole pairs bound together and have been a subject of interest within semiconductor physics since the 1930s.[8] Furthermore, recent

Received: February 28, 2025
Revised: June 11, 2025
Accepted: June 16, 2025

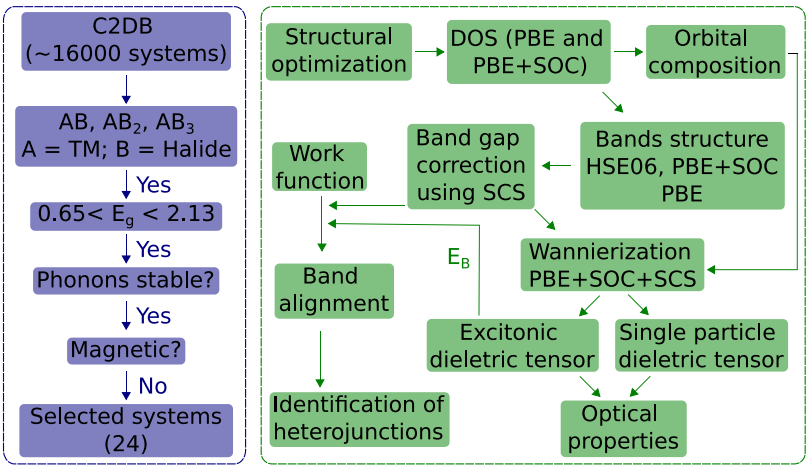

Figure 1. Flowchart illustrating the procedures implemented for the screening of the 2D TMHs (left panel) compounds alongside the framework (right panel) to investigate their optical and excitonic properties.

investigations into 2D materials have renewed interest due to the effects of quantum confinement and weak dielectric screening, thereby resulting in the formation of strongly bound excitons.[9] These excitons demonstrate binding energies that are one to 2 orders of magnitude greater than those encountered in three-dimensional (3D) semiconductors.[10] Excitons in TMDs can be classified into bright excitons (optically accessible) and dark excitons (optically inaccessible), the latter being further classified as spin-forbidden or momentum-forbidden transitions. Studies on TMDs have also revealed additional types of excitons, such as localized and interlayer excitons.[11]

Motivated by advancements in the 2D materials research field, 2D transition metal halides (TMHs) are regarded as a promising family of materials for various applications, such as photocatalysis and quantum cutting,[12] photovoltaics,[13] photodetectors,[14] thermoelectric applications,[15] and ultrafast photonics.[16] Our work aims to provide a perspective on optoelectronic applications for this less explored class of layered materials, offering insights into future applications involving excitonic effects. These materials comprise transition metal (A) and halide (B = Cl, Br, and I) elements, being represented by the following chemical formula A_mB_n. The literature reports various stoichiometries for TMHs, with most experimental studies focusing on AB_2 and AB_3,[17] including RhI_3, PbI_2, and BiI_3. Additionally, AB TMHs, such as CuBr and gadolinium monohalides, have also been investigated experimentally.[18,19]

TMHs are often synthesized via mechanical exfoliation, facilitated by their layered structure in which the layers are held together by van der Waals (vdW) forces, similar to those found in graphene and TMDs. For example, exfoliated RhI_3 flakes obtained from the vdW-bonded bulk structure remain stable under ambient conditions for up to two months.[20] Theoretical calculations also reveal lower exfoliation energy for monolayers of GeI_2 than for graphite, highlighting the feasibility of mechanical exfoliation for producing monolayers.[21] Additional methods, including liquid phase and vapor phase deposition, have also been extensively reported for TMH synthesis.[14,16,18,22]

Furthermore, research on excitonic properties in TMHs has revealed intriguing phenomena, including the coupling between excitonic and magnetic properties, layer-dependent properties, and excitonic effects in Janus and heterostructures,[23,24] however, consideration of those effects remains unaddressed for many compositions. Moreover, semiconducting TMH compounds have shown potential for integrating photovoltaic devices[12,13,25,26] as the presence of chemical halide species should facilitate their integration with halide perovskites (HPVK), which have recently shown promise for use in photovoltaic applications with the advantages of low cost and high efficiency[27] despite stability improvements when exposed to operational conditions of moisture and heat is still a demand. The strategy of combining HPVKs and 2D materials[28] has the potential to overcome these instability issues, and the excitonic properties of 2D TMHs should be relevant in this context.

In this work, we explore 2D TMHs with various crystal structures, compositions, and stoichiometries, selecting the most promising candidates for optical applications while accounting for excitonic effects. Initially, the compositions for examination were chosen after a systematic search of the Computational 2D Materials Database (C2DB). Subsequently, 24 selected materials were investigated employing a combination of Density Functional Theory (DFT) simulations, the Tight-Binding (TB) approach, and the Bethe−Salpeter Equation (BSE) to scrutinize the significance of excitonic effects on their optoelectronic properties. Despite good agreement between our results for the equilibrium lattice parameters and electronic spectra compared to those reported in the C2DB data set, we found significant deviations in the electronic properties of particular compositions. These discrepancies arise primarily from spin−orbit coupling (SOC) and hybrid exchange−correlation calculations using the HSE06 functional, which we attribute to implementation differences among the computational codes.

We found that excitonic effects significantly impact optoelectronic properties; our results reveal exciton binding energies ranging from 0.23 to 0.81 eV. In particular, TiI_2 in the $P\bar{6}m2$ space group emerges as a potential excitonic insulator (EI).[29] Furthermore, the presence of excitons influences the absorption spectra, systematically reducing the maximum absorption coefficient for all systems. This reduction affects transitions across the infrared, visible, and ultraviolet regions, depending on the composition. Finally, we classified all possible heterojunctions using Anderson's rule and observed

https://doi.org/10.1021/acsaem.5c00610
ACS Appl. Energy Mater. XXXX, XXX, XXX−XXX

changes in the heterojunction type when comparing the independent particle approximation (IPA) against BSE simulations, including a reduction in the number of type II heterojunctions. These findings highlight the critical role of excitonic effects in evaluating the optical potential of TMHs.

2. THEORETICAL APPROACH AND COMPUTATIONAL DETAILS

To fulfill our goals, the selection of potential 2D TMH materials was carried out using the C2DB,[30] with a focus on their electronic properties. The selected 2D TMHs were characterized by DFT calculations, e.g., equilibrium lattice parameters, electronic structure evaluation, work function, etc. Furthermore, the optical properties of these systems were evaluated through the computation of real and imaginary dielectric functions, while excitonic properties were ascertained using Hamiltonian parametrization within the TB framework, utilizing maximally localized Wannier function techniques. Subsequently, the BSE was solved to examine the excitonic properties. The integration of all these techniques is depicted in Figure 1, where the workflow is also explicitly defined. The following subsections provide a summary of the theoretical approach and the computational details of the principal steps.

2.1. Total Energy Calculations. Our calculations are based on the DFT framework,[31,32] as implemented in the Vienna *Ab initio* Simulation Package (VASP), version 5.4.4.[33−35] In this framework, interactions between valence and core electrons are described using the Projector Augmented Wave (PAW) method,[36] while plane waves expand the single particle Kohn−Sham wave functions.

All equilibrium structures were obtained using the semilocal formulation Perdew−Burke−Ernzerhof (PBE)[37] for the exchange−correlation energy functional (E_{XC}), which produces results consistent with experimental studies.[38] Due to the presence of heavy elements, our simulations include SOC effects for the valence states to improve the description of the electronic states, which affects the evaluation of the density of states, electronic band structure, and the entire TB parametrization procedure, including decomposition of states in the valence and conduction bands. Furthermore, improved electronic band gap values were obtained by incorporating the Heyd−Scuseria−Ernzerhof (HSE06) hybrid exchange-correlation functional[39] within the scissor operator approach. This evaluation of electronic structure provides band gap values close to the experimental results due to minimizing self−interaction errors[40] while incorporating electronic band splittings resulting from SOC.

Due to the high computational cost of using the hybrid HSE06 functional in conjunction with SOC, we employed the scissor operator (χ) approach to correct the electronic band gap values (E_g) and adjust the entire electronic band structure. This correction was applied by rigidly shifting all electronic states in the conduction band by χ, calculated using the following equation

$$E_g = E_g^{\mathrm{PBE+SOC,dir}} + \overbrace{(E_g^{\mathrm{HSE06,dir}} - E_g^{\mathrm{PBE,dir}})}^{\chi} \quad (1)$$

Here, $E_g^{x,\mathrm{dir}}$, where x = PBE+SOC, HSE06, or PBE, represents the optical band gap evaluated using the PBE+SOC, HSE06, and PBE approximations, respectively.

While the scissor operator methodology provides a computationally affordable way to correct band gap values, it does not extend to the Kohn−Sham wave functions. This limitation poses a challenge for accurately modeling band dispersion (or effective masses) and heterostructures, where charge redistribution and the emergence of an electric dipole between monolayers may occur. More sophisticated approaches, such as the GW approximation, can yield accurate band structures. However, GW methods are sensitive to several factors, including the specific variant used (e.g., treatment of the Coulomb potential, self-consistency schemes),[41,42] the inclusion of spin−orbit coupling,[43] and the choice of the starting point for quasiparticle calculations.[44] Despite these complexities, the scissor operator remains a valuable tool for identifying trends in excitonic and optical properties, and for evaluating the role of exciton binding energies in band gap classification at a manageable computational cost.

2.2. Optimization Procedures and Computational Parameters. The equilibrium 2D structures were obtained by optimizing the stress tensor within the *xy* plane while keeping the vacuum thickness frozen to those from C2DB, and the atomic forces in all directions, using a cutoff energy of $2\times\mathtt{ENMAX}_{max}$ for truncate the plane wave expansion in order to minimize the Pulay stress. Here, $\mathtt{ENMAX}_{max}$ is the maximum cutoff energy recommended for the atomic species contained in the selected TMHs (Cl, Br, I, Ti, Co, Zr, Mo, Rh, Pd, Hf, W and Hg) within each PAW projector (i.e., 262.472, 216.285, 175.647, 383.774, 323.400, 346.364, 344.914, 247.408, 250.925, 282.964, 317.132, and 312.028 eV). The equilibrium structures were obtained once the atomic force in each atom was smaller than 0.01 eV/Å, with an electronic self−consistency total energy criterion of 10^{-6} eV.

We employed the Monkhorst−Pack scheme[45] for Brillouin zone integration, determining the number of subdivisions in the in−plane reciprocal space using a **k**-point length of R_k = 25 Å and a Gaussian smearing of 0.05 eV for structural optimizations and for generating the overlap and hoping parameter for expansion in terms of Maximally Localized Wannier Functions (Section 2.3). For the remaining properties, a cutoff energy of $1.125\times\mathtt{ENMAX}_{max}$ was used, while R_k was increased to 50 Å, and the Gaussian smearing was reduced to 0.01 eV. The Section S3.3. Supporting Information (SI) includes the plane-wave cutoff energies and **k**-point grids used for each system in this work.

2.3. Optical and Excitonic Properties. We employ the Maximally Localized Wannier Function (MLWF)[46] method, as implemented in the Wannier90 software,[47,48] to parametrize the electronic Hamiltonian to study the optical and excitonic properties. The resulting TB Hamiltonian is expressed as follows

$$H\mathbf{Rk}) = H_0 + \sum_{i=1}^{N} e^{\mathbf{ik}\cdot\mathbf{R}_i} H_{\mathbf{R}i} \quad (2)$$

where H_0 represents the TB Hamiltonian matrix elements between orbitals in the unit cell, containing hopping and on-site parameters; and $H_{\mathbf{R}_i}$ includes hopping parameters between the unit cell and neighboring cells indexed by translational vectors $\mathbf{R}_i$.

From the parametrized TB Hamiltonian, the WanTiBEXOS (a Wannier-based tight-binding code for electronic band structures),[49] calculates the optical and excitonic properties by solving the BSE. Previous reports have successfully applied the same methodology to investigate various 2D materials[50]

https://doi.org/10.1021/acsaem.5c00610
ACS Appl. Energy Mater. XXXX, XXX, XXX−XXX

Table 1. Step−by−step Summary of the Screening Procedure Used to Select 2D Transition-metal Halide Compounds from the C2DB Data Set (16905 Compounds)

	AB			AB_2			AB_3			
step	Cl	Br	I	Cl	Br	I	Cl	Br	I	total
step 1: TMH composition	55	57	54	97	95	99	49	45	46	597
step 2: SQ over 20%	1	2	3	15	13	14	9	5	6	68
step 3: strong phonon stability	0	0	1	14	12	10	8	3	5	53
step 4: non−magnetic	0	0	1	6	5	7	3	0	2	24

and low-dimensional perovskites.[51] The solution of the BSE, as depicted in eq 3, provides excitonic properties.

$$(E_{c,\mathbf{k}} - E_{v,\mathbf{k}})A^n_{c,v,\mathbf{k}} + \frac{1}{\Omega N_{\mathbf{k}}} \times \sum_{\mathbf{k}',v',c'} W_{(\mathbf{k},v,c),(\mathbf{k}',v',c')}A^n_{c',v',\mathbf{k}'} = E^n A^n_{c,v,\mathbf{k}} \quad (3)$$

where c (v) represents conduction (valence) states, $E_{c,\mathbf{k}}$ ($E_{v,\mathbf{k}}$) denotes the single−particle energies at each $\mathbf{k}$−point for conduction (valence) bands, $A^n_{c,v,\mathbf{k}}$ stands for the exciton wavevector, E_n indicates the n−th exciton energy, Ω signifies the volume of the unit cell, and $N_{\mathbf{k}}$ denotes the number of $\mathbf{k}$−points. $W_{(\mathbf{k},\,v,\,c),\,(\mathbf{k}',\,v',\,c')}$ represents the 2D truncated Coulomb matrix, as proposed by Rozzi et al.[52] The optical properties in both IPA and BSE were calculated from the dielectric tensor, as shown in Section S3.8 of the SI.

2.4. Screening Procedure to Select 2D Transition Metal Halides from the C2DB Data Set. The selection of 2D TMHs was conducted through a systematic examination of specific properties within the C2DB database, utilizing a four-step methodology, see Table 1: (i) identification of structures with stoichiometries AB, AB_2, or AB_3, where A denotes transition metals and B corresponds to Cl, Br, or I; (ii) analysis of structures with band gaps determined via the HSE06 XC functional, incorporating SOC, within the range of 0.65 to 2.13 eV, thereby ensuring the efficiency of materials for p−n junctions exceeding the Shockley−Queisser (SQ) limit of 20%; (iii) selection of materials demonstrating high phonon stability; and (iv) preference for nonmagnetic systems, owing to the inadequacies of the scissors operator correction in magnetic systems, attributed to disparate spin channel corrections,[53] and its lack of consideration for interactions between spin channels. Thus, a total of 24 two-dimensional compounds were identified, representing a broad spectrum of TMH compounds, which includes compounds with stoichiometries of AB (1), AB_2 (18), and AB_3 (5), wherein the numerals within parentheses signify the respective counts of identified compounds.

3. RESULTS AND DISCUSSION

For clarity in the discourse of our results, this section is systematically arranged as follows: Section 3.1 initially addresses the initial structures derived from C2DB, which subsequently underwent optimization within the framework of DFT calculations, as elucidated in Section 3.2. Sections 3.3, 3.4 and 3.5 expounds on the ground state electronic structures, encompassing the density of states, the influence of SOC on electronic properties, and the adjustment of the band gap. Sections 3.6 and 3.7 elucidates the optical and excitonic properties related to the TB Hamiltonian and the resolution of the BSE. Finally, in Section 3.8 we present the bands alignment and the heterojunction classification, including the role of excitonic effect.

3.1. Structural and Compositional Characterization of Transition-Metal Halides. Figure 2 presents a stick-and-ball representation of the crystalline structures, along with the chemical formulas and the number of unit cells for each species listed per space group (SG). As mentioned, a total of 24 materials were identified, each exhibiting a range of crystalline structures and compositions. Notably, one material is characterized by the AB stoichiometry within the $P\bar{3}m1$ space group, while 18 are categorized as AB_2 with SGs $P2_1|m$, $P\bar{6}m2$, $P2_1|c$, and $P\bar{3}m1$. Furthermore, five materials manifest the AB_3 stoichiometry within SGs $P\bar{3}1m$ and $P\bar{6}2m$. Mercury-based TMHs exhibit structures within the same space group regardless of their stoichiometries; these are denoted HgI_2 and Hg_2I_2 by $P\bar{3}m1$-α and $P\bar{3}m1$-β, respectively. The selected structures possess either hexagonal or tetragonal

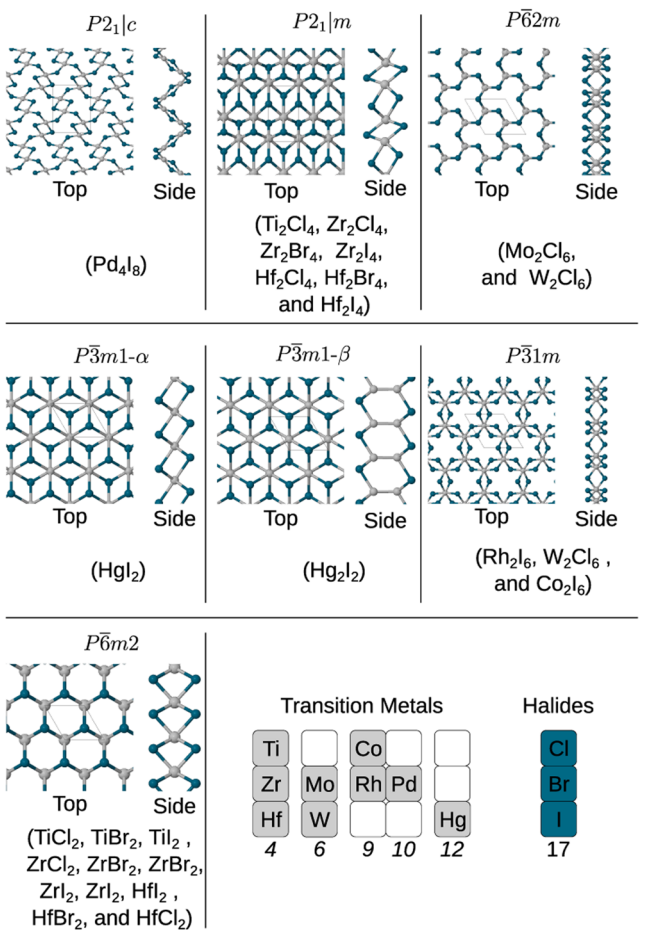

Figure 2. Summary of the selected structures in this work provided in both top and side views, along with their respective compositions.

https://doi.org/10.1021/acsaem.5c00610
ACS Appl. Energy Mater. XXXX, XXX, XXX−XXX

Bravais lattices, all of which exhibit point-inversion symmetry. Consequently, dipole corrections are not required due to the negligible net dipole moment in the systems studied. On the other hand, symmetry-breaking effects may serve as a useful avenue for probing novel electronic or structural phenomena in future investigations.

The selected TMHs encompass a broad spectrum of TM species, incorporating groups 4, 6, 9, 10, and 12 of the periodic table, as illustrated in Figure 2. Additionally, given that halides generally possess an oxidation number (NOX) of −1, the titanium- and palladium-based TMHs exhibit a NOX of +2 for the AB_2 stoichiometry. Similarly, Co_2I_6 shows a NOX of +3. Mercury-based TMHs are characterized by NOX values of +1 and +2 for Hg_2I_2 and HgI_2, respectively, which are the predominant oxidation states for these metals. In contrast, zirconium-based TMHs have NOX of +2, Mo_2Cl_6 is associated with NOX of +3, while hafnium- and tungsten-based TMHs have NOX values of +2 and +3, respectively, which are atypical oxidation states.

Nonetheless, it is important to note that our approach may overlook materials with potentially interesting properties, as we excluded those with small and large band gaps and magnetic characteristics. However, since our focus is on high-performance materials for optoelectronic applications, we target those with high maximum efficiencies under the Shockley−Queisser (SQ) limit and exclude magnetic materials, as their properties can be sensitive to environmental conditions such as external magnetic fields.

3.2. Equilibrium Lattice Parameters and Structural Trends. Table 2 summarizes the optimized in-plane lattice parameters (a_0 and b_0) for all selected TMH compounds, comparing our calculated parameters with data from the C2DB database and additional theoretical results for validation. Our optimized geometric parameters demonstrate excellent concordance with the C2DB, exhibiting a maximum deviation from the lattice parameter of merely 0.07 Å (or 0.8%). This robust consistency extends to the structural angles and space groups, underscoring the reliability of our optimization methodology. Compared to other studies in the literature, most of our lattice parameters show deviations of less than 0.03 Å (or 0.49%). Slightly larger deviations were observed for Pd_4I_8 (up to 0.09 Å or 1.34%) compared to Yekta et al.,[55] and for Co_2I_6 (up to 0.08 Å or 0.88%) compared to Zhang et al.[57] This high degree of agreement across multiple sources substantiates the validity of our equilibrium geometry calculations. For all subsequent calculations, the structures remain fixed in these optimized equilibrium geometries.

Furthermore, the examination of the equilibrium lattice parameters uncovers several significant trends. A direct correlation with halogen size emerges consistently: the lattice parameters typically increase as the halogen atom's size increases for a given transition metal. This phenomenon is evident in the Titanium series ($TiCl_2$, $TiBr_2$, TiI_2), where a_0 for $P\bar{6}m2$ structures expands from approximately 3.28 Å (Cl) to 3.77 Å (I). The space group symmetry also significantly influences the lattice parameters. In particular, materials within the $P\bar{6}m2$ space group (e.g., $TiCl_2$, $ZrCl_2$) demonstrate nearly identical in-plane lattice parameters ($a_0 \approx b_0$), a feature indicative of hexagonal symmetry. In contrast, structures belonging to the $P2_1|m$ space group (e.g., Ti_2Cl_4, Zr_2Cl_4) exhibit distinctly different lattice parameters ($a_0 \neq b_0$), with b_0 being substantially larger than a_0, a mark of lower (monoclinic) symmetry.

Table 2. In−Plane Lattice Parameters (a_0 and b_0) of Optimized Structure, from C2DB and Results Presented in the Literature[a]

composition	this work		C2DB		literature		
space group	a_0 (Å)	b_0 (Å)	a_0 (Å)	b_0 (Å)	refs	a_0 (Å)	b_0 (Å)
Ti_2Cl_4 ($P2_1\|m$)	3.25	5.91	3.25	5.91	13	3.24	5.90
$TiCl_2$ ($P\bar{6}m2$)	3.28	3.28	3.28	3.28	54	3.29	3.29
$TiBr_2$ ($P\bar{6}m2$)	3.47	3.47	3.47	3.47			
TiI_2 ($P\bar{6}m2$)	3.76	3.77	3.77	3.76			
Co_2I_6 ($P\bar{3}1m$)	6.72	6.74	6.74	6.72	55	6.81	6.81
Zr_2Cl_4 ($P2_1\|m$)	3.33	6.23	3.33	6.24	26	3.34	6.23
$ZrCl_2$ ($P\bar{6}m2$)	3.41	3.41	3.41	3.41			
Zr_2Br_4 ($P2_1\|m$)	3.49	6.50	3.49	6.50	26	3.49	6.48
$ZrBr_2$ ($P\bar{6}m2$)	3.56	3.56	3.56	3.56			
Zr_2I_4 ($P2_1\|m$)	3.76	6.91	3.77	6.91	26	3.76	6.91
ZrI_2 ($P\bar{6}m2$)	3.82	3.83	3.83	3.82			
Mo_2Cl_6 ($P\bar{6}2m$)	5.59	5.59	5.59	5.59			
Rh_2I_6 ($P\bar{3}1m$)	6.90	6.93	6.93	6.90	56	6.92	6.92
Pd_4I_8 ($P2_1\|c$)	7.13	9.10	7.17	9.03	57	7.14	9.02
Hf_2Cl_4($P2_1\|m$)	3.27	6.16	3.28	6.16	58	3.26	6.13
					25	3.27	6.14
$HfCl_2$ ($P\bar{6}m2$)	3.35	3.35	3.35	3.35			
Hf_2Br_4 ($P2_1\|m$)	3.43	6.43	3.44	6.42	25	3.43	6.42
					15	3.43	6.41
$HfBr_2$ ($P\bar{6}m2$)	3.49	3.50	3.50	3.49			
Hf_2I_4 ($P2_1\|m$)	3.70	6.83	3.72	6.81	25	3.71	6.81
HfI_2 ($P\bar{6}m2$)	3.76	3.77	3.77	3.76			
W_2Cl_6 ($P\bar{3}1m$)	5.56	5.56	5.56	5.56			
W_2Cl_6 ($P\bar{6}2m$)	5.52	5.52	5.52	5.52			
Hg_2I_2 ($P\bar{3}m1$)	4.46	4.48	4.46	4.47			
HgI_2 ($P\bar{3}m1$)	4.37	4.39	4.39	4.37			

[a]The formula is shown with the total number of atoms. SG stands for space group.

Moreover, the identity of the TM species also affects the lattice parameters. In the evaluation of TMHs that possess identical halogens and analogous space groups (as exemplified by $TiCl_2$, $ZrCl_2$, $HfCl_2$ in $P\bar{6}m2$), it is observed that the lattice parameters generally increase as one moves down the transition metal group (as noted in the series from Ti to Zr to Hf), which aligns with the trend of increasing atomic radii. In addition, stoichiometry also plays a role. Compounds exhibiting varied stoichiometries, including the A_2B_6 series (for instance, Mo_2Cl_6, W_2Cl_6) as well as mercury-based TMH (e.g., Hg_2I_2 and HgI_2), exhibit larger lattice parameters in comparison to the AB_2 compounds, thereby reflecting their unique structural configurations and bonding properties. Together, these observations underscore the complex relationship between the chemical composition, crystal structure, and fundamental lattice dimensions inherent in these transition-metal halides.

3.3. Orbital Contributions from Density of States. An in-depth characterization of the electronic states was performed through analysis of both total and local densities of states (DOS and LDOS, respectively) for all selected 2D compounds. The DOS selected for examination are presented in Figure 3, with the remaining results compiled in the Supporting Information. Most of the systems investigated exhibit predominant contributions from the *d*-states associated with the transition metals (TM) and the *p*-states of the halide atoms proximal to the maximum valence band, as depicted in

https://doi.org/10.1021/acsaem.5c00610
ACS Appl. Energy Mater. XXXX, XXX, XXX−XXX

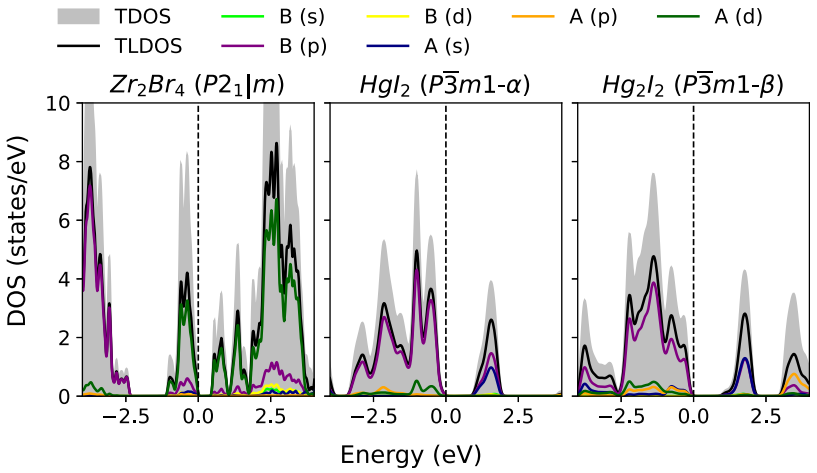

Figure 3. Total and local density of states (DOS and LDOS, respectively) for the 2D Zr_2Br_4, HgI_2, and Hg_2I_2 compounds calculated with the DFT-PBE+SOC framework. The total (local) DOS, is denoted as T(L)DOS, whereas A(s, p, d) and B(s, p, d) represent the decomposition of the local DOS transition metals (A) and halides (B) species, respectively. The vertical dashed line indicates the valence band maximum.

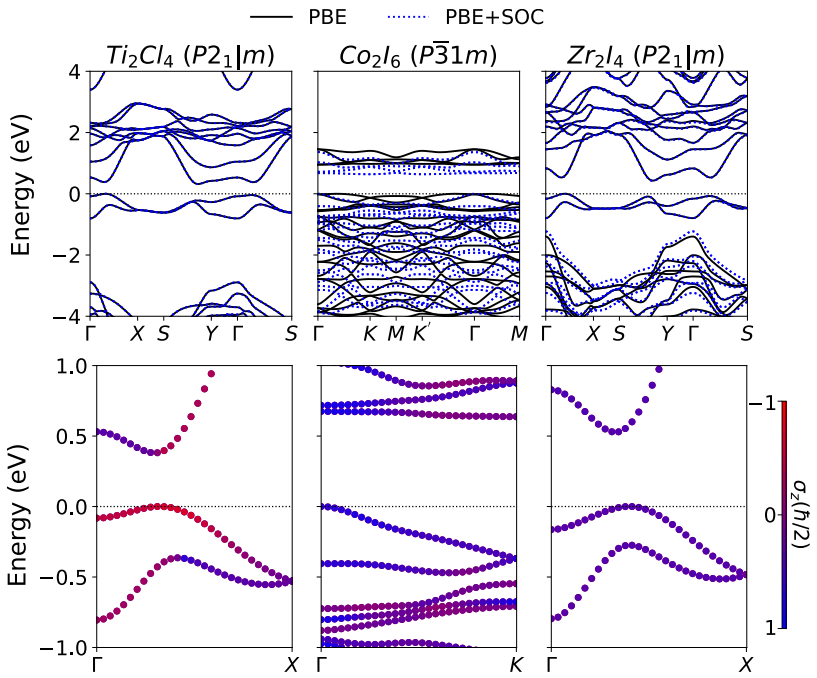

Figure 4. Top panel: PBE (black solid lines) and PBE+SOC (blue dashed lines) bands structures for Ti_2Cl_4 ($P2_1|m$), Co_2I_6 ($P\bar{3}1m$) and Zr_2I_4 ($P2_1|m$) showcase the bands' structures where (i) the SOC effect not change the band structure, (ii) changes in the band gap and (iii) changes in states apart from VBM and CBM in states between −4 and 4 eV. Low panel: spin-projection in up and down components (σ_z) close to direct band gap of these materials.

the left panel of Figure 3. Notable exceptions are observed for mercury-based TMHs. For example, as referenced in HgI_2, the primary contributions emerge from the states s- and p-states, while in Hg_2I_2, the p-states of both TM and the halides predominate, as illustrated in the middle and right panels of Figure 3.

In addition to our computational findings, previous research has corroborated significant contributions from the halide *p*-states and the TM *d*-states. For example, Tang et al.[59] identified significant *p*-orbital contributions in $TiCl_2$ utilizing the HSE06 functional, while Huang et al.[13,26] and Zhang et al.[57] reported analogous results for titanium-, zirconium-, hafnium-, and palladium-based TMHs.

The representation of the electronic states using maximally localized Wannier functions (MLWFs) was performed based on PBE+SOC results and atomic state characterization derived from density of states calculations. Comparisons between the results obtained from the PBE and PBE+SOC approximations, as elaborated in Section 3.4, revealed only minor variations in DOS and orbital composition near the maximum of the valence band. Further analysis of the DOS suggests that accurate construction of MLWFs generally requires the inclusion of s-, p-, and d-orbitals for both transition metals and halides. However, there are exceptions for compounds such as TiI_2, Mo_2Cl_6, and W_2Cl_6 within the $P\bar{6}2m$ space group, where only p- and d-orbitals were considered for halide atoms.

https://doi.org/10.1021/acsaem.5c00610
ACS Appl. Energy Mater. XXXX, XXX, XXX−XXX

Furthermore, in the case of W_2Cl_6 within the $P\bar{3}1m$ space group, s-, p-, d- and f-orbitals were incorporated.

3.4. Role of Spin−Orbit Coupling in the Electronic Structure. This section highlights the main changes in the electronic structure resulting from the inclusion of spin−orbit coupling (SOC). The first row of Figure 4 illustrates three distinct behaviors observed in calculations performed using PBE and PBE+SOC, across an energy range of 4 eV above and below the VBM level. First, some systems show only minor changes within this energy window, as demonstrated by the left panel in the first row of Figure 4 for Ti_2Cl_4. This behavior is also observed in $TiCl_2$, Zr_2Cl_4, $ZrCl_2$ (within the space groups $P2_1/m$ and $P\bar{6}m2$, respectively), and Mo_2Cl_6.

In other systems, the SOC causes breaks in the valence (VB) and conduction (CB) bands and alters the band gap value, as exemplified by Co_2I_6 in the middle panel (first row) of Figure 4. This behavior was also observed for Rh_2I_6, Pd_4I_8, tungsten−based, and mercury−based TMHs. The SOC induces changes up to 0.38 eV in both the fundamental and direct band gaps for W_2Cl_6 ($P\bar{3}1m$), for example. For Co_2I_6, the conduction band minimum (CBM) shifts from the $\Gamma-K$ path to the Γ point when SOC is included in the PBE calculations (that is, from PBE to PBE+SOC). Furthermore, a significant change in electronic states is observed along the $K-M$ direction.; conversely, the opposite holds for the valence band maximum (VBM), while the band gap value of this material remains indirect. The same was observed for Rh_2I_6. For Pd_4I_8 and tungsten-based TMHs, we observed band splits at some points and a reduction in the band gap; however, without changes to the VBM or CBM points. In contrast, mercury-based TMHs exhibited no significant alterations in the shape of the bands but suffered a reduction in the band gap. Finally, in the remaining systems, there is no change in the band gap; however, changes occur in states apart from VB and CB, as shown in the right panel (top row) of Figure 4 for Zr_2I_4 as an example. In particular, we found that the effect of SOC becomes stronger as the atomic numbers of species in the structure increase, consistent with the expectation that relativistic effects grow stronger for heavier elements with more electronic shells. For example, when comparing the SOC effects for $TiCl_2$, $TiBr_2$, and TiI_2, we observe an increase in SOC-induced splits as the halogen atoms become heavier. This trend can also be observed in other structures.

Finally, in the bottom row of Figure 4 we showcase the σ_z spin projection for the same sampling systems as highlighted above near the direct band gap. We observed that for Ti_2Cl_4, the direct band gap includes a spin-forbidden transition which can impact the optical spectra. It is worthwhile to include SOC effects, as it changes the bands' dispersion which can impact its properties, mainly in heavy atoms. For instance, the SOC can introduce spin-forbidden optical transitions, as discussed below, splits in bands dispersion which alter the material's optical response, as observed for TMDs,[60] changes in bands edges, which can impact the bands alignment and heterojunction types, and finally changes in fundamental gap character (direct or indirect) as in indirect band gap materials the selection rules introduce some momentum-forbidden transitions.

3.5. Electronic Band Gaps: Correction, Validation, and Functional Dependence. Although the PBE calculation provides good results for structural parameters, as discussed in Section 3.2, it underestimates the band gap, which impacts the correct description of electronic transitions in optical and excitonic calculations. Consequently, this section outlines the band gap correction performed using the scissors operator methodology, as described in Section 2.1. Figure 5 presents the

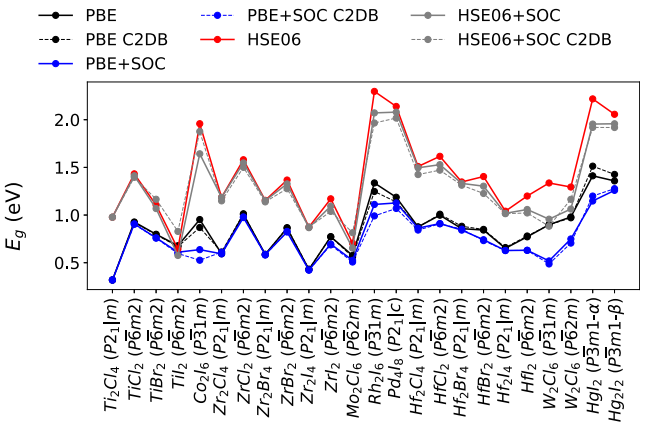

Figure 5. Optical electronic band gaps using several approximations: PBE, PBE+SOC, HSE06, and PBE+SOC+χ (HSE06+SOC) with the scissors operator. The PBE, PBE+SOC, and HSE06+SOC values reported within the C2DB database[30] are reported for comparison.

direct band gaps of our calculations using the PBE, PBE+SOC, and HSE06 functionals along with the corrected band gap for comparison with the values PBE, PBE+SOC, and HSE06+-SOC obtained from C2DB.

The corrected band gaps range from 0.59 up to 2.39 eV. Here, the scissors operator in our systems corrects the band gaps from −0.04 for TiI_2 up to 0.97 eV, as is the case with Pd_4I_8. The corrected band gap shows some differences from those calculated by C2DB. Specifically, the discrepancies in Ti_2Cl_4 and $ZrCl_2$ are less than 1%. In contrast, the deviations for Zr_2Br_4, $ZrBr_2$, Zr_2I_4, ZrI_2, Rh_2I_6, Pd_4I_8, Hafnium, and mercury−based TMHs range from 1 to 5%. Meanwhile, the remaining systems exhibit deviations above 5%. The differences are more pronounced (above 10%) for $TiCl_2$ (11.3%), $TiBr_2$ (19.9 eV), TiI_2 (39.6%), Co_2I_6 (18.1%), and Mo_2Cl_6 (24.8%). Consequently, although our optimized structures align with those of C2DB, the electronic properties display significant deviations, primarily due to the hybrid functional calculations, as the discrepancies observed are larger than those seen in PBE and PBE+SOC calculations.

Several theoretical works also investigated band gaps with various levels of approximation. For example, according to Huang et al.[13] the monolayer Ti_2Cl_4 features a fundamental band gap of 0.99 eV within the HSE06 functional while our simulations deliver 0.98 eV. For zirconium−based TMHs in $P21|m$ SG, Huang et al.[26] calculated band gaps using the HSE06 functional of 1.15, 1.14, and 0.85 eV for Zr_2Cl_4, Zr_2Br_4, and Zr_2I_4 while our results are 1.19, 1.15, and 0.87 eV, respectively. For Zr_2Cl_4, Wang et al.[61] calculated a direct fundamental band gap of 0.62 eV with the PBE functional along the $\Gamma-X$ points, which aligns with our findings. However, discrepancies arise for HSE06 band gaps; that is, while we obtained an indirect fundamental band gap of 1.19 eV, they reported a direct fundamental gap of 1.27 eV. For Rh_2I_6, Wu et al.[56] calculated a band gap of 1.33 eV with the PBE functional, which aligns well with our value of 1.34 eV. For Pd_4I_8, Zhang et al.[57] obtained band gaps of 1.18 eV (PBE) and 2.15 eV (HSE06), which are close to our values of 1.19 eV (PBE), and 2.14 eV (HSE06). For hafnium−based TMHs

https://doi.org/10.1021/acsaem.5c00610
ACS Appl. Energy Mater. XXXX, XXX, XXX−XXX

within the SG $P21|m$ (Hf_2Cl_4, Hf_2Br_4, and Hf_2I_4), Huang et al.[25] calculated band gaps of 1.47, 1.34, and 1.03 eV, while our results are 1.52, 1.35, and 1.04 eV, respectively, all using the HSE06 functional. Li et al.[58] also studied the Hf_2Cl_4 reporting band gaps of 0.87 (PBE) and 1.48 eV (HSE06), which is in agreement with our findings of 0.88 (PBE) and 1.52 eV (HSE06) for Hf_2Cl_4. Lastly, Fan et al.[15] reported a band gap of 1.31 eV for Hf_2Br_4 using the HSE06 functional.

However, it is well-known that the HSE06 functional underestimates the band gaps in wide band gap semiconductors[62] and for two-dimensional materials[63] compared to the GW method. For example, comparing our corrected band gaps with those obtained using the G_0W_0 method from C2DB, we observed that our calculations underestimated the band gaps by an average of 0.41 eV, as presented in Table S9 of the SI. Despite that, the computations of electronic structure using GW methods can also be challenging as they depend on several factors, as discussed in Section 2.1.

3.6. Exciton Binding Energy, Ground State, Bright State, and Trends. Table 3 summarizes the calculated exciton ground-state energy (E_X^{GS}), binding energy (E_b), and bright-state energy (E_X^{br}) for all selected 24 2D TMH materials. A bright state is defined here as one with an absorption coefficient greater than 1×10^{-3} cm^{-1}. The exciton binding energies, which represent the differences between the electronic band gaps and the first excitonic states, range from 0.23 to 0.81 eV. These values are comparable or larger to other 2D materials such as WS_2 (0.32 eV)[10] and MoS_2 (0.24 eV),[64] black phosphorus (ranging from 0.213 to 0.106 eV for 2 to 6 layers),[65] and $PdSeO_3$ (0.6 eV).[66]

Table 3. Exciton Ground State (E_X^{GS}), Exciton Binding Energy (E_b), and Bright Exciton State (E_X^{br}) Energy

system	E_X^{GS} (eV)	E_b (eV)	E_X^{br} (eV)
Ti_2Cl_4 ($P2_1|m$)	0.25	0.78	0.40
$TiCl_2$ ($P\bar{6}m2$)	0.65	0.81	0.65
$TiBr_2$ ($P\bar{6}m2$)	0.34	0.73	0.34
TiI_2 ($P\bar{6}m2$)	−0.01	0.62	0.03
Co_2I_6 ($P\bar{3}1m$)	0.90	0.73	0.90
Zr_2Cl_4 ($P2_1|m$)	0.67	0.55	0.67
$ZrCl_2$ ($P\bar{6}$ $m2$)	1.43	0.74	1.43
Zr_2Br_4 ($P2_1|m$)	0.63	0.59	0.63
$ZrBr_2$ ($P\bar{6}m2$)	1.30	0.75	1.30
Zr_2I_4 ($P2_1|m$)	0.30	0.58	0.30
ZrI_2 ($P\bar{6}m2$)	0.96	0.68	0.96
Mo_2Cl_6 ($P\bar{6}2m$)	0.36	0.29	0.36
Rh_2I_6 ($P\bar{3}1m$)	1.26	0.74	1.26
Pd_4I_8 ($P2_1|c$)	1.62	0.47	1.62
Hf_2Cl_4 ($P2_1|m$)	1.05	0.45	1.05
$HfCl_2$ ($P\bar{6}m2$)	1.67	0.73	1.67
Hf_2Br_4 ($P2_1|m$)	0.92	0.52	0.92
$HfBr_2$ ($P\bar{6}m2$)	1.44	0.71	1.44
Hf_2I_4 ($P2_1|m$)	0.53	0.51	0.53
HfI_2 ($P\bar{6}m2$)	1.19	0.64	1.19
W_2Cl_6 ($P\bar{3}1m$)	0.59	0.36	0.59
W_2Cl_6 ($P\bar{6}2m$)	0.84	0.23	0.84
HgI_2 ($P\bar{3}m1$-α)	1.59	0.65	1.59
Hg_2I_2 ($P\bar{3}m1$-β)	1.69	0.28	1.69

For most systems, E_X^{GS} is identical to E_X^{br}, implying that the lowest-energy exciton is often bright or the energy difference is negligible. However, titanium-halide series, i.e., Ti_2Cl_4, $TiCl_2$, $TiBr_2$, and TiI_2 are exceptions. Specifically, Ti_2Cl_4 exhibits an optically inactive (dark) excitonic ground state, differing from its bright state by 0.15 eV. This is likely due to a spin-forbidden transition, as the VBM has a major spin-down projection and the CBM a major spin-up projection as pointed out in Section 3.4. All remaining systems, except Ti_2Cl_4 and TiI_2 (discussed below), show ground states brightly active.

A consistent trend observed across titanium-, zirconium-, and hafnium-based halide systems is a decrease in both E_X^{GS} and E_X^{br} as the halogen is varied from Cl to Br to I. This trend suggests that heavier halides promote exciton formation at lower energies. For example, in the TiX_2 series, E_X^{GS} drops from 0.65 eV for $TiCl_2$ to 0.34 eV for $TiBr_2$, reaching a notably low value of − 0.01 eV for TiI_2. A similar decreasing trend is observed in the ZrX_2 and HfX_2 series. In contrast, the trend in E_b values as a function of halogen species is more complex. For Zr and Ti halides, E_b slightly decreases or remains nearly constant. In contrast, for Hf halides, E_b exhibits either a slight increase in the Hf_2X_4 compounds or a decrease in the HfX_2 compounds.

Generally, as the atomic number of the metal increases (Ti → Zr → Hf), E_X^{GS} and E_X^{br} tend to increase for comparable stoichiometries and halogens. This indicates larger band gaps or higher exciton excitation energies in materials with heavier metal centers. For example, E_X^{GS} increases from 0.65 eV for $TiCl_2$ to 1.43 eV for $ZrCl_2$ and 1.67 eV for $HfCl_2$. The trend for E_b with changes in metals is less consistent, varying with halogen. However, for the M_2X_4 series, E_b appears to decrease from Ti to Zr to Hf. Furthermore, MX_2 compounds generally exhibit higher E_X^{GS} and E_X^{br} values compared to their M_2X_4 counterparts, indicating a larger excitonic energy gap in the MX_2 stoichiometry. For example, $TiCl_2$ has an E_X^{GS} of 0.65 eV versus 0.25 eV for Ti_2Cl_4. The E_b also follows this trend; i.e., MX_2 compounds have higher values compared to M_2X_4 in the Ti, Zr, and Hf TMHs series.

The most striking observation is the negative value E_X^{GS} of −0.01 eV for TiI_2, which is very unusual for an exciton ground state. This could suggest a unique property of the material, such as an EI, where the exciton binding energy exceeds the material's band gap.[29] However, the effect is weak as the exciton ground state is close to the VBM and could change to the forbidden region by thermal effects or dielectric screening. Nevertheless, several mechanisms, such as strain can be explored to enhance this effect. Many other systems have E_b values typically between 0.5 and 0.8 eV, suggesting a common range of interaction strengths. Finally, the table highlights how polymorphism affects excitonic properties. For W_2Cl_6, phase $P\bar{6}2m$ shows a higher E_X^{GS} and E_X^{br} but a lower E_b than phase $P\bar{3}1m$. Similarly, in HgI_2, the $P\bar{3}m1$-α phase has a higher E_b than the $P\bar{3}m1$-β phase, even with similar values of E_X^{GS} and E_X^{br}. These variations emphasize the sensitivity of excitonic behavior to subtle differences in the crystal structure. It is important to acknowledge that the exciton energies obtained in this work may deviate by approximately 100 meV from those calculated with more stringent computational settings. This level of variation is expected given the trade-off between computational cost and accuracy, and remains within an acceptable range for the present analysis. This deviation aligns with our expectations based on the employed methodology, as elucidated in Section S6.1 of the SI.

3.7. Optical Absorption Coefficient. Figure 6 presents the optical absorption coefficient for all systems studied in IPA

https://doi.org/10.1021/acsaem.5c00610
ACS Appl. Energy Mater. XXXX, XXX, XXX−XXX

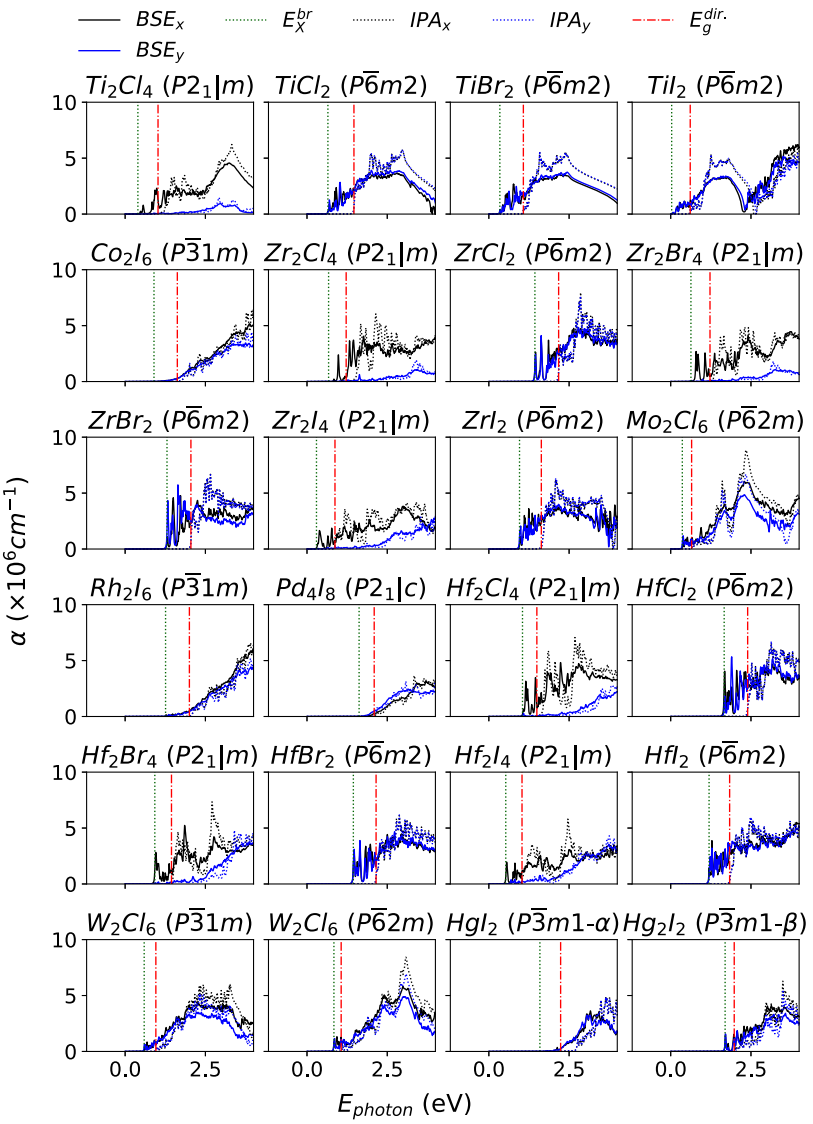

Figure 6. Absorption coefficient (α) as a function of photon energy (E_{photon}) considering the IPA (BSE) calculations in the x and y directions parallel to the monolayer, $IPA_{x,y}$ ($BSE_{x,y}$). The vertical dashed red line is the excitonic ground state, the vertical green dotted the exciton bright state (calculated as states with absorption coefficient above 10^3 cm^{-1}), and the direct band gap (red dotted and dashed line).

and by the solution of BSE alongside the parallel directions of the monolayers.

3.7.1. Isotropic and Nonisotropic Light Absorption. First, all tetragonal structures exhibit nonisotropic light absorption. In contrast, hexagonal structures, including those with space groups $P\bar{3}1m$ and $P\bar{6}2m$, as well as structures with space group $P\bar{6}m2$ and HgI_2 within the $P\bar{3}m1-\alpha$ space group, display isotropic light absorption spectra in both IPA and BSE calculations. Although BSE calculations introduce some differences in the optical absorption spectra, they do not alter the isotropic or non−isotropic behavior, as observed in other 2D materials.[50]

3.7.2. Role of Excitonic Effects. Given that the exciton bright state lies in the forbidden band, the consideration of excitons results in lowering the optical offset up to 0.81 eV, as depicted by the green dotted lines in Figure 6. Some systems have a clear excitonic signature with isolated peaks below the band gap, as in the case of TMH based on $TiCl_2$, $TiCl_2$, zirconium- and hafnium-based TMHs where, in these systems, we observed that the excitonic peak presents an absorption coefficient at least 1/3 the maximum absorption coefficient in both the IPA and BSE calculations. Specifically, in the case of $ZrBr_2$ and $HfCl_2$, the peak is almost the maximum absorption peak of IPA, both in the $P\bar{6}m2$ space group. However, the opposite holds for Co_2I_6, Rh_2I_6, Pd_4I_8, Hg_2I_2 and for the TMH based on Tungsten.

3.7.3. Trends in Maximum Absorption Coefficient. This section focuses on the analysis of the maximum absorption coefficient, which provides information on the maximum interaction of the material with sunlight. It is calculated within a photon energy range from 0 up to 4 eV, representing an energy interval that covers the infrared to ultraviolet spectrum of sunlight. Figure 7 presents the maximum absorption coefficient (top panel) as its correspondent photon energy (bottom panel). For all systems, the IPA absorption coefficient exceeds the BSE ones, where we observed differences 3.1×10^6 cm^{-1} for $ZrCl_2$. The maximum absorption coefficient considering the excitons is close to or larger than those experimentally observed for other 2D materials, such as MoS_2[67] (2.8×10^6 cm^{-1}).

https://doi.org/10.1021/acsaem.5c00610
ACS Appl. Energy Mater. XXXX, XXX, XXX−XXX

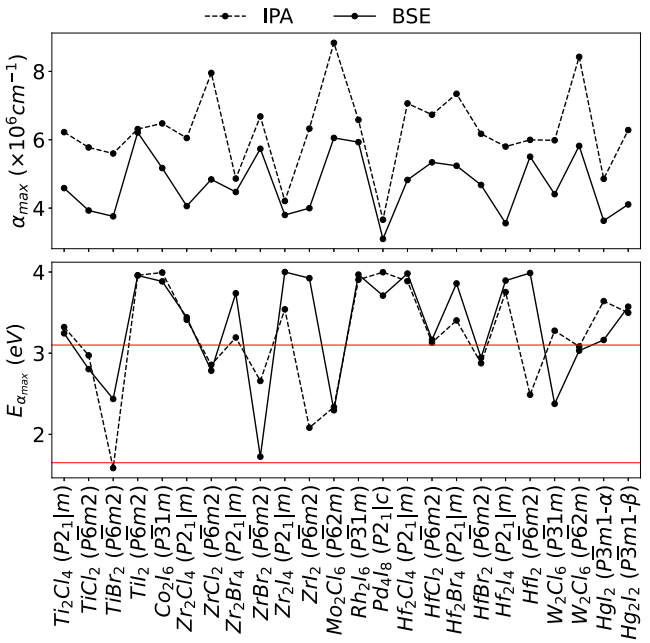

Figure 7. Maximum absorption coefficient (upper panel) and corresponding photon energy (bottom panel) for IPA (dashed line) and BSE (solid line) calculations. The red solid lines on the horizontal in the bottom panel delimit the energies of the visible spectrum.

The photon energy of the maximum absorption coefficient also varies in behavior, as it covers a wide range of light spectra, from infrared, as in the case of $TiBr_2$ from IPA calculations up to ultraviolet spectra, for most materials in both the IPA and BSE frameworks. The photon energy also differs from IPA to BSE calculations for almost all systems, except for TiI_2. For example, the most notable case is the W_2Cl_6 ($P\bar{3}1m$) where the maximum absorption changes from the ultraviolet spectrum (IPA) to the visible spectra (BSE), while the opposite holds for HfI_2 and ZrI_2. For $TiBr_2$, it changes from infrared in IPA to visible spectra for BSE calculations.

3.8. Band Alignment and Heterojunction Classification: The Role of Excitonic Effects. To investigate the feasibility of these materials for device applications, the electronic structure of potential bilayer heterojunctions was assessed under conditions of low interlayer binding, as illustrated in Figure 8. The upper panel shows the CBM, the VBM, and the bright state of the exciton results, using the vacuum level as the reference zero energy, derived by calculating the Hartree potential within the vacuum region, as discussed in the Section S4.6 of SI. The lower panel categorizes the potential heterojunctions within the frameworks of the independent particle approximation (IPA) and the BSE framework based on Anderson's rule,[68] culminating in a total of 276 possible heterojunctions.

Our analysis elucidates distinct patterns in band alignment. With respect to the VBM, as the halogen transitions from Cl to Br to I (descending the group), the VBM exhibits an upward shift (becoming less negative, or approaching the vacuum level) for a specific metal and stoichiometry, signifying a reduction in the ionization potential of the material. Similarly, as the metal increases in atomic mass (Ti → Zr → Hf), the VBM also tends to shift upward.

Additionally, MX_2 compounds typically feature a higher VBM (less negative) relative to M_2X_4 compounds composed of the same metal and halogen. Analogous trends are identified

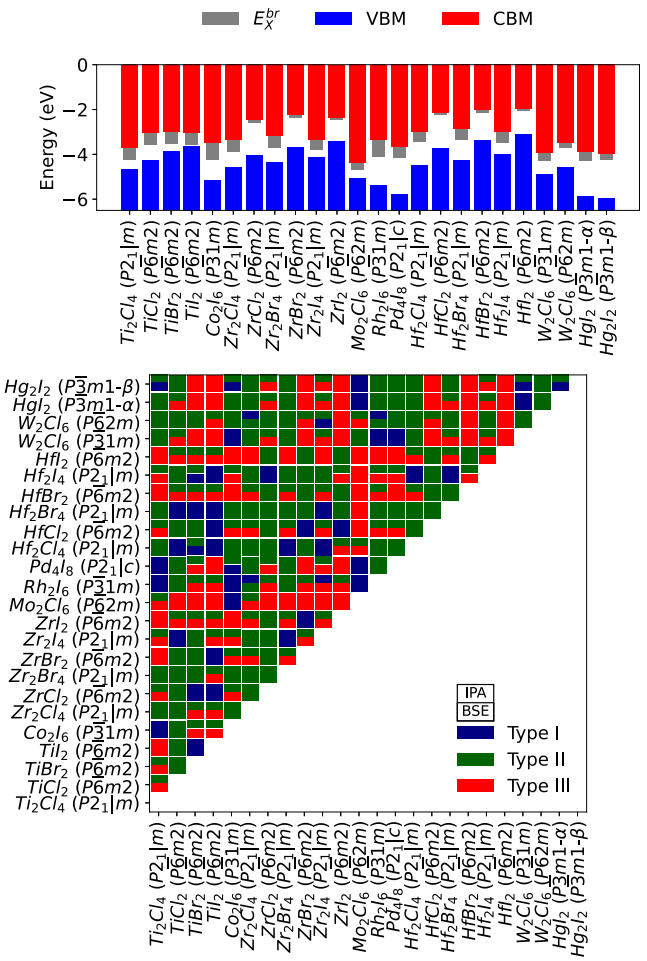

Figure 8. Top panel presents the alignment of the electronic VBM, CBM, and the excitonic bright state (E_X^{br}) with respect to the vacuum level. The lower panel shows the possible heterojunctions evaluated from Anderson's rule within both IPA and BSE frameworks. The squares in the intersection between the materials in the axis represent the character of the heterojunction, where the upper part represents the character considering IPA and the lower part the BSE calculations. Also, the blue color represents type I, the green represents type II, and the red type III heterojunctions.

for the CBM: it generally shifts upward (becomes less negative) as the halogen atomic mass increases from Cl → Br, indicating a decline in electron affinity, however, it decreases from Br → I. We also observe that the CBM and upward (becomes less negative) as the metal becomes heavier, suggesting an decrease of electron affinity. MX_2 compounds also generally possess a higher CBM than M_2X_4 compounds. The bright exciton state, represented by the gray bars (E_X^{br}), corresponding to the energy gap between the CBM and the bright exciton state, exhibits significant variability between the systems, aligning with the varied exciton binding energies documented in Table 3. The total electronic band gap, as represented by the energy difference between VBM and CBM, typically increases with heavier metals (Ti → Zr → Hf) and contracts with heavier halogens (Cl → Br → I), with MX_2 compounds generally exhibiting larger gaps than M_2X_4 compounds.

Based on IPA calculations, the identification of 39 potential type I, 183 type II, and 54 type III heterojunctions was achieved. This classification is illustrated in detail in the lower

https://doi.org/10.1021/acsaem.5c00610
ACS Appl. Energy Mater. XXXX, XXX, XXX−XXX

panel of Figure 8. Type I heterojunctions (dark blue), characterized by the VBM and CBM of one material being enclosed by those of another, frequently occur, particularly in cases involving Ti_2Cl_4 and TiI_2, which implies relatively elevated energy alignments. Type II heterojunctions (green) are the most common, underscoring their extensive potential for facilitating charge separation across material interfaces. In contrast, type III heterojunctions (red), with their distinct overlapping band gaps, are observed less frequently, but are present, particularly in combinations involving Mo_2Cl_6 and W_2Cl_6 as well as selected iodide compounds.

On the contrary to the results derived from IPA, the BSE calculations reveal changes in the classification of heterojunctions, specifically to 133 type I, 100 type II, and 43 type III categories. The incorporation of excitonic effects within the BSE framework precipitates the reclassification of 90 heterostructures into various types (I, II, or III). In particular, 3 systems transition from type I to type II, 8 systems shift from type II to type I, and 78 systems are reclassified from type II to type III as they progress from IPA to BSE calculations. In contrast, 35, 97, and 54 heterostructures persist in their classifications as type I, type II, and type III, respectively, across both IPA and BSE computational approaches. These marked reclassifications, especially the numerous transitions from type II to type III, underscore the critical importance of excitonic effects in the precise determination of heterojunction types and their subsequent implications for device development. The marked presence of type II heterojunctions within both IPA and BSE frameworks, albeit with varying specific numbers, highlights the intrinsic suitability of these materials for applications that advantageously exploit the spatially separated electron and hole populations.

The origin of these changes when excitonic effects are included can be summarized as follows: (i) Type I to II: In the IPA, both the valence band maximum (VBM) and conduction band minimum (CBM) are localized in the same layer of the heterostructure, characterizing a Type I alignment. However, when excitonic effects are included, the bright exciton localized in the other layer may shift in energy and cross above the CBM or below the E_X^{br} of the other layer, resulting in a transition to Type II alignment. (ii) Type II to I: Initially, the VBM is localized in one layer and the CBM in the other, indicating a staggered (Type II) band alignment. Upon inclusion of excitonic effects, both the bright exciton transition and the VBM wave function localize within the same layer, and the exciton energy E_X^{br} becomes enclosed by the band edges of that layer, giving rise to a Type I alignment. (iii) Type II to III: In this case, excitonic corrections shift the bright exciton energy of one material into the valence band of the other, producing a broken-gap (Type III) alignment, even though the IPA indicates a staggered configuration.

4. KEY INSIGHTS FROM EXCITON ANALYSIS

Given the relevance of excitonic effects in 2D materials—characterized by larger exciton binding energies than their three-dimensional (3D) counterparts due to quantum confinement—an extended analysis of these effects in transition metal halides, a less-explored class of 2D materials, remains unprecedented. However, exciton properties are sensitive to both temperature and dielectric screening, which are not considered in the present study, introducing a quantitative limitation when assessing performance under device-relevant conditions. For example, it has been shown that as the dielectric screening increases, the exciton binding energy decreases. Furthermore, temperature induces phonon screening and originates nonradiative decay paths, causing a redshift of exciton energies and an increase in absorption line widths for certain excitonic states.[69,70]

In our study, we observed that the exciton binding energy ranges from 0.23 to 0.81 eV, a value closer to and higher than the exciton binding energy typically observed in 2D materials, such as transition metal dichalcogenides, black phosphorus and $PdSeO_3$. Among these, we observed three distinct behaviors: (i) Materials that have a fundamental state dark, which means that the state cannot be accessed by optical excitations. Specifically, the case of Ti_2Cl_4 where the exciton binding energy is 0.78 eV, while the difference between the electronic band gap and the fist excitonic bright state (optically accessible) is 0.63 eV. (ii) The EI, where the excitonic ground state lies in the valence band, specifically the case of TiI_2, with possess an exciton bright state energy 0.03 eV. (iii) Systems with the exciton ground state bright, as the case of the remaining materials.

This implies that when the IPA is compared with the BSE, consideration of the excitonic effects is crucial for an accurate description of the optical band gaps of these materials. Apart from changes in the optical band gap, the consideration of excitonic effects also alters the light absorption spectra. For instance, the shape of the absorption coefficient spectra is changed and the maximum absorption coefficient is decreased for all systems. We also observed changes in photon energy corresponding to the maximum absorption coefficient. These changes are of particular importance for some systems, specifically $TiBr_2$, ZrI_2, HfI_2, and W_2Cl_6 within the spacegroup $P\bar{3}1m$, where changes in spectra were observed between the infrared, visible, and ultraviolet regions.

Finally, when possible heterojunctions are evaluated, excitonic effects must be taken into account, which alters the evaluated type of heterojunction between two semiconductors. Of the 276 possible heterojunctions in total, 90 altered their character with the inclusion of excitonic effects, in contrast to calculations based on IPA. Given our interest in photovoltaic applications, we focus here on type -II heterojunctions. In particular, the number of type II heterojunctions decreases when contrasting the IPA and BSE methodologies, with eight structures changing from type II to I and 78 from type II to III, while 97 remains the same.

Thus, the excitonic effects observed here are noteworthy, including the (i) large exciton binding energy; (ii) changes in the optical absorption coefficient, the maximum absorption coefficient, and the corresponding photon energy; and (iii) variations in possible heterojunctions, emphasizing the importance of considering excitonic properties when evaluating the optical properties of the TMH family of 2D materials.

5. CONCLUSIONS

In conclusion, this article explores the 2D TMHs, including an analysis of structural, electronic, optical, and excitonic properties, as well as band alignment for optical applications, particularly photovoltaics. Based on the structures collected from C2DB, in our simulations, we observed a good agreement concerning structural parameters, consistent with C2DB and other works in the literature. However, significant deviations were noted in electronic properties, primarily due to spin−orbit coupling and hybrid functional calculations, specifically the HSE06 functional.

https://doi.org/10.1021/acsaem.5c00610
ACS Appl. Energy Mater. XXXX, XXX, XXX−XXX

Our calculations reveal that the excitonic effects play a major role in determining the optical properties of the 2D TMHs studied here, aligning with the findings for other 2D materials. Specifically, we observed an exciton binding energy ranging from 0.23 to 0.81 eV, where TiI_2 within the space group $P\bar{6}m2$ features an excitonic insulator behavior, while the remaining materials feature a fundamental excitonic state that is optically accessible (bright), except Ti_2Cl_4 within the space group $P2_1/m$ which has a fundamental excitonic state that is optically inaccessible (dark).

The excitonic effects also play an important role in optical absorption, where we observe changes in the spectra and in the maximum absorption spectra, accompanied by a corresponding change in photon energy. We observed that the maximum absorption coefficient decreases for all systems, while the corresponding photon energy also changes; some systems exhibit a shift in the corresponding spectrum region between infrared, visible, and ultraviolet when comparing the BSE and IPA frameworks. Finally, consideration of excitonic effects is also relevant for calculating possible heterojunctions for optical applications, as several possible heterojunctions change their character between IPA and BSE calculations.

■ ASSOCIATED CONTENT

Data Availability Statement

The authors declare no competing financial interest. As mentioned, all DFT calculations were performed using the Vienna Ab initio Simulation Package (VASP), which is available under a non−free academic license. Further details can be found at https://www.vasp.at/. The wannierization procedure was carried out using the Wannier90 package, distributed under the GPLv2 license, with additional information available at https://wannier.org/. Finally, the optical and excitonic properties were analyzed using the WanTiBEXOS: a Wannier−based tight−binding code designed for electronic band structure, excitonic, and optoelectronic properties of solids. WanTiBEXOS is available under the GPLv3 license, and further details can be accessed at https://github.com/ac-dias/wantibexos. Furthermore, additional details are provided within the electronic Supporting Information, while additional input and output of all data can be obtained under the url https://data.mendeley.com/ and all the crude data can be obtained directly with the authors under request.

Supporting Information

The Supporting Information is available free of charge at https://pubs.acs.org/doi/10.1021/acsaem.5c00610.

Additional details of the screaming procedure; PAW projectors; computational convergence tests; example of INCAR input file for VASP; additional details for wannierization procedure; tight binding framework; quasiparticle simulations; dielectric tensor calculations; additional results from DFT calculations; wannierization; and additional details on excitonic and optical properties (PDF)

■ AUTHOR INFORMATION

Corresponding Author

Matheus P. Lima − *Department of Physics, Federal University of São Carlos, 13565-905 São Carlos, SP, Brazil;* orcid.org/0000-0001-5389-7649; Email: mplima@df.ufscar.br

Authors

Natan M. Regis − *Department of Physics, Federal University of São Carlos, 13565-905 São Carlos, SP, Brazil;* orcid.org/0000-0003-1097-3036

Juarez L. F. Da Silva − *São Carlos Institute of Chemistry, University of São Paulo, 13560-970 São Carlos, SP, Brazil;* orcid.org/0000-0003-0645-8760

Complete contact information is available at: https://pubs.acs.org/10.1021/acsaem.5c00610

Funding

The Article Processing Charge for the publication of this research was funded by the Coordenacao de Aperfeicoamento de Pessoal de Nivel Superior (CAPES), Brazil (ROR identifier: 00x0ma614).

Notes

The authors declare no competing financial interest.

■ ACKNOWLEDGMENTS

The authors gratefully acknowledge support from FAPESP (São Paulo Research Foundation, Grant Numbers 2017/11631-2, 2018/21401-7), Shell and the strategic importance of the support given by ANP (Brazil's National Oil, Natural Gas and Biofuels Agency) through the R&D levy regulation. M.P.L. gratefully acknowledges financial support from the CNPq (Brazilian National Council for Scientific and Technological Development) Grand Number 314169/2023-7 and FAPESP, project No. 2024/08610-7. This study was financed in part by the National Counsel for Technological and Scientific Development (fellowships for Natan Moreira Regis).

■ REFERENCES

(1) Novoselov, K. S.; Geim, A. K.; Morozov, S. V.; Jiang, D.; Zhang, Y.; Dubonos, S. V.; Grigorieva, I. V.; Firsov, A. A. Electric Field Effect in Atomically Thin Carbon Films. *Science* **2004**, *306*, 666−669.

(2) Randviir, E. P.; Brownson, D. A. C.; Banks, C. E. A decade of graphene research: production, applications and outlook. *Mater. Today* **2014**, *17*, 426−432.

(3) Manzeli, S.; Ovchinnikov, D.; Pasquier, D.; Yazyev, O. V.; Kis, A. 2D transition metal dichalcogenides. *Nat. Rev. Mater.* **2017**, *2*, No. 17033.

(4) Splendiani, A.; Sun, L.; Zhang, Y.; Li, T.; Kim, J.; Chim, C.-Y.; Galli, G.; Wang, F. Emerging Photoluminescence in Monolayer MoS_2. *Nano Lett.* **2010**, *10*, 1271−1275.

(5) Radisavljevic, B.; Radenovic, A.; Brivio, J.; Giacometti, V.; Kis, A. Single-layer MoS_2 transistors. *Nat. Nanotechnol.* **2011**, *6*, 147−150.

(6) Bertolazzi, S.; Krasnozhon, D.; Kis, A. Nonvolatile Memory Cells Based on MoS_2/Graphene Heterostructures. *ACS Nano* **2013**, *7*, 3246−3252.

(7) Tsai, M.-L.; Su, S.-H.; Chang, J.-K.; Tsai, D.-S.; Chen, C.-H.; Wu, C.-I.; Li, L.-J.; Chen, L.-J.; He, J.-H. Monolayer MoS_2 Heterojunction Solar Cells. *ACS Nano* **2014**, *8*, 8317−8322.

(8) Frenkel, J. On the Transformation of light into Heat in Solids. I. *Phys. Rev.* **1931**, *37*, 17−44.

(9) Mueller, T.; Malic, E. Exciton physics and device application of two-dimensional transition metal dichalcogenide semiconductors. *npj 2D Mater. Appl.* **2018**, *2*, No. 17033.

(10) Chernikov, A.; Berkelbach, T. C.; Hill, H. M.; Rigosi, A.; Li, Y.; Aslan, B.; Reichman, D. R.; Hybertsen, M. S.; Heinz, T. F. Exciton Binding Energy and Nonhydrogenic Rydberg Series in Monolayer WS_2. *Phys. Rev. Lett.* **2014**, *113*, No. 076802.

(11) Tonndorf, P.; Schmidt, R.; Schneider, R.; Kern, J.; Buscema, M.; Steele, G. A.; Castellanos-Gomez, A.; Zant, H. S. J. v. d.; Vasconcellos, S. M. d.; Bratschitsch, R. Single-photon emission from

localized excitons in an atomically thin semiconductor. *Optica* **2015**, *2*, 347−352.
(12) Huang, X.; Yan, L.; Zhou, Y.; Wang, Y.; Song, H.-Z.; Zhou, L. Group 11 Transition-Metal Halide Monolayers: High Promises for Photocatalysis and Quantum Cutting. *J. Phys. Chem. Lett.* **2021**, *12*, 525−531.
(13) Huang, X.; Yan, L.; Zhou, Y.; Zhang, W.; Xie, X.; Xu, Q.; Wang, Y.; Zhou, L.; Song, H.TiX_2 (X = *Cl*, *Br*, *I*) monolayer and type II heterostructures as promising efficient solar cells. In *International Conference on Optoelectronic and Microelectronic Technology and Application* 2020; pp 578−583 .
(14) Wang, Y.; Gan, L.; Chen, J.; Yang, R.; Zhai, T. Achieving highly uniform two-dimensional PbI_2 flakes for photodetectors via space confined physical vapor deposition. *Sci. Bull.* **2017**, *62*, 1654−1662.
(15) Fan, Q.; Yang, J.; Wang, N. Theoretical Prediction of the Monolayer Hf_2Br_4 as Promising Thermoelectric Material. *Materials* **2022**, *15*, 4120.
(16) Fan, Q.; Huang, J.; Dong, N.; Hong, S.; Yan, C.; Liu, Y.; Qiu, J.; Wang, J.; Sun, Z. Liquid Exfoliation of Two-Dimensional PbI_2 Nanosheets for Ultrafast Photonics. *ACS Photonics* **2019**, *6*, 1051−1057.
(17) Miró, P.; Audiffred, M.; Heine, T. An atlas of two-dimensional materials. *Chem. Soc. Rev.* **2014**, *43*, 6537−6554.
(18) Gong, C.; Chu, J.; Yin, C.; Yan, C.; Hu, X.; Qian, S.; Hu, Y.; Hu, K.; Huang, J.; Wang, H.; Wang, Y.; Wangyang, P.; Lei, T.; Dai, L.; Wu, C.; Chen, B.; Li, C.; Liao, M.; Zhai, T.; Xiong, J. Self-Confined Growth of Ultrathin 2D Nonlayered Wide-Bandgap Semiconductor CuBr Flakes. *Adv. Mater.* **2019**, *31*, No. 1903580.
(19) Chen, C.; Fang, L.; Zhao, G.; Liu, X.; Wang, J.; Burton, L. A.; Zhang, Y.; Ren, W. A high-temperature quantum anomalous Hall effect in electride gadolinium monohalides. *J. Mater. Chem. C* **2021**, *9*, 9539−9544.
(20) Wang, F.; Zhang, Z.; Zhang, Y.; Nie, A.; Zhao, W.; Wang, D.; Huang, F.; Zhai, T. Honeycomb RhI_3 Flakes with High Environmental Stability for Optoelectronics. *Adv. Mater.* **2020**, *32*, No. 2001979.
(21) Liu, C.-S.; Yang, X.-L.; Liu, J.; Ye, X.-J. Exfoliated Monolayer GeI_2: Theoretical Prediction of a Wide-Band Gap Semiconductor with Tunable Half-Metallic Ferromagnetism. *J. Phys. Chem. C* **2018**, *122*, 22137−22142.
(22) Li, J.; Guan, X.; Wang, C.; Cheng, H.-C.; Ai, R.; Yao, K.; Chen, P.; Zhang, Z.; Duan, X.; Duan, X. Synthesis of 2D Layered BiI_3 Nanoplates, BiI_3/WSe_2 van der Waals Heterostructures and Their Electronic, Optoelectronic Properties. *Small* **2017**, *13*, No. 1701034.
(23) Zhao, X.; Liu, F.; Ren, J.; Qu, F. Valleytronic and magneto-optical properties of Janus and conventional $TiBrI/CrI_3$ and TiX_2/CrI_3 (X = *Br*, *I*) heterostructures. *Phys. Rev. B* **2021**, *104*, No. 085119.
(24) Grzeszczyk, M.; Acharya, S.; Pashov, D.; Chen, Z.; Vaklinova, K.; van Schilfgaarde, M.; Watanabe, K.; Taniguchi, T.; Novoselov, K. S.; Katsnelson, M. I.; Koperski, M. Strongly Correlated Exciton-Magnetization System for Optical Spin Pumping in $CrBr_3$ and CrI_3. *Adv. Mater.* **2023**, *35*, No. 2209513.
(25) Huang, X.; Zhou, L.; Yan, L.; Wang, Y.; Zhang, W.; Xie, X.; Xu, Q.; Song, H.-Z. $HfX2$ (X = *Cl*, *Br*, *I*) Monolayer and Type II Heterostructures with Promising Photovoltaic Characteristics. *Chin. Phys. Lett.* **2020**, *37*, No. 127101.
(26) Huang, X.; Zhuo, Z.; Yan, L.; Wang, Y.; Xu, N.; Song, H.-Z.; Zhou, L. Single-Layer Zirconium Dihalides ZrX_2 (X = *Cl*, *Br*, and *I*) with Abnormal Ferroelastic Behavior and Strong Anisotropic Light Absorption Ability. *J. Phys. Chem. Lett.* **2021**, *12*, 7726−7732.
(27) Jena, A. K.; Kulkarni, A.; Miyasaka, T. Halide Perovskite Photovoltaics: Background, Status, and Future Prospects. *Chem. Rev.* **2019**, *119*, 3036−3103.
(28) Zhang, Z.; Wang, S.; Liu, X.; Chen, Y.; Su, C.; Tang, Z.; Li, Y.; Xing, G. Metal Halide Perovskite/2D Material Heterostructures: Syntheses and Applications. *Small Methods* **2021**, *5*, No. 2000937.
(29) Jérome, D.; Rice, T. M.; Kohn, W. Excitonic Insulator. *Phys. Rev.* **1967**, *158*, 462−475.
(30) Gjerding, M. N.; Taghizadeh, A.; Rasmussen, A.; Ali, S.; Bertoldo, F.; Deilmann, T.; Knøsgaard, N. R.; Kruse, M.; Larsen, A. H.; Manti, S.; Pedersen, T. G.; Petralanda, U.; Skovhus, T.; Svendsen, M. K.; Mortensen, J. J.; Olsen, T.; Thygesen, K. S. Recent progress of the Computational 2D Materials Database (C2DB). *2D Mater.* **2021**, *8*, No. 044002.
(31) Hohenberg, P.; Kohn, W. Inhomogeneous Electron Gas. *Phys. Rev.* **1964**, *136*, B864.
(32) Kohn, W.; Sham, L. J. Self-Consistent Equations Including Exchange and Correlation Effects. *Phys. Rev.* **1965**, *140*, No. A1133.
(33) Kresse, G.; Hafner, J. Ab initio molecular dynamics for open-shell transition metals. *Phys. Rev. B* **1993**, *48*, No. 13115.
(34) Kresse, G.; Furthmüller, J. Efficiency of Ab-Initio Total Energy Calculations for Metals and Semiconductors Using a Plane-Wave Basis Set. *Comput. Mater. Sci.* **1996**, *6*, 15−50.
(35) Kresse, G.; Furthmüller, J. Efficient iterative schemes for ab initio total-energy calculations using a plane-wave basis set. *Phys. Rev. B* **1996**, *54*, No. 11169.
(36) Kresse, G.; Joubert, D. From ultrasoft pseudopotentials to the projector augmented-wave method. *Phys. Rev. B* **1999**, *59*, 1758−1775.
(37) Perdew, J. P.; Burke, K.; Ernzerhof, M. Generalized Gradient Approximation Made Simple. *Phys. Rev. Lett.* **1996**, *77*, 3865.
(38) Yuk, S. F.; Sargin, I.; Meyer, N.; Krogel, J. T.; Beckman, S. P.; Cooper, V. R. Putting Error Bars on Density Functional Theory. *Sci. Rep.* **2024**, *14*, No. 20219.
(39) Heyd, J.; Scuseria, G. E.; Ernzerhof, M. Hybrid functionals based on a screened Coulomb potential. *J. Chem. Phys.* **2003**, *118*, 8207−8215.
(40) Perdew, J. P.; Zunger, A. Self-interaction correction to density-functional approximations for many-electron systems. *Phys. Rev. B* **1981**, *23*, 5048−5079.
(41) Thygesen, K. S. Calculating excitons, plasmons, and quasiparticles in 2D materials and van der Waals heterostructures. *2D Mater.* **2017**, *4*, No. 022004.
(42) Acharya, S.; Pashov, D.; Cunningham, B.; Rudenko, A. N.; Rösner, M.; Grüning, M.; van Schilfgaarde, M.; Katsnelson, M. I. Electronic structure of chromium trihalides beyond density functional theory. *Phys. Rev. B* **2021**, *104*, No. 155109.
(43) Mohebpour, M. A.; Tagani, M. B. First-Principles Study on the Electronic and Optical Properties of AlSb Monolayer. *Sci. Rep.* **2023**, *13*, No. 9925.
(44) Pela, R. R.; Vona, C.; Lubeck, S.; Alex, B.; Gonzalez Oliva, I.; Draxl, C. Critical Assessment of G_0W_0 Calculations for 2D Materials: The Example of Monolayer MoS_2. *npj Comput. Mater.* **2024**, *10*, No. 77.
(45) Monkhorst, H. J.; Pack, J. D. Special points for Brillouin-zone integrations. *Phys. Rev. B* **1976**, *13*, 5188.
(46) Marzari, N.; Mostofi, A. A.; Yates, J. R.; Souza, I.; Vanderbilt, D. Maximally localized Wannier functions: Theory and applications. *Rev. Mod. Phys.* **2012**, *84*, 1419−1475.
(47) Mostofi, A. A.; Yates, J. R.; Pizzi, G.; Lee, Y.-S.; Souza, I.; Vanderbilt, D.; Marzari, N. An updated version of wannier90: A tool for obtaining maximally-localised Wannier functions. *Comput. Phys. Commun.* **2014**, *185*, 2309−2310.
(48) Pizzi, G.; Vitale, V.; Arita, R.; Blügel, S.; Freimuth, F.; Géranton, G.; Gibertini, M.; Gresch, D.; Johnson, C.; Koretsune, T.; Ibañez-Azpiroz, J.; Lee, H.; Lihm, J.-M.; Marchand, D.; Marrazzo, A.; Mokrousov, Y.; Mustafa, J. I.; Nohara, Y.; Nomura, Y.; Paulatto, L.; Poncé, S.; Ponweiser, T.; Qiao, J.; Thöle, F.; Tsirkin, S. S.; Wierzbowska, M.; Marzari, N.; Vanderbilt, D.; Souza, I.; Mostofi, A. A.; Yates, J. R. Wannier90 as a community code: new features and applications. *J. Phys.: Condens. Matter* **2020**, *32*, No. 165902.
(49) Dias, A. C.; Silveira, J. F. R. V.; Qu, F. WanTiBEXOS: AWannier based Tight Binding code for electronic band structure, excitonic and optoelectronic properties of solids. *Comput. Phys. Commun.* **2023**, *285*, No. 108636.

https://doi.org/10.1021/acsaem.5c00610
ACS Appl. Energy Mater. XXXX, XXX, XXX−XXX

(50) Querne, M. B. P.; Dias, A. C.; Janotti, A.; Da Silva, J. L. F.; Lima, M. P. Tuning Excitonic Properties of Monochalcogenides via Design of Janus Structures. *J. Phys. Chem. C* **2024**, *128*, 12164−12177.
(51) Ozório, M. S.; Dias, A. C.; Silveira, J. F. R. V.; Da Silva, J. L. F. Theoretical Investigation of the Role of Anion and Trivalent Cation Substitution in the Physical Properties of Lead-Free Zero-Dimensional Perovskites. *J. Phys. Chem. C* **2022**, *126*, 7245−7255.
(52) Rozzi, C. A.; Varsano, D.; Marini, A.; Gross, E. K. U.; Rubio, A. Exact Coulomb cutoff technique for supercell calculations. *Phys. Rev. B* **2006**, *73*, No. 205119.
(53) Dias, A. C.; Bragança, H.; de Mendonça, J. P. A.; Da Silva, J. L. F. Excitonic Effects on Two-Dimensional Transition-Metal Dichalcogenide Monolayers: Impact on Solar Cell Efficiency. *ACS Appl. Energy Mater.* **2021**, *4*, 3265−3278.
(54) Wang, Y.; Huang, P.; Liu, J.; Peng, H.; Zou, Y.; Chu, H.; He, Y.; Xu, F.; Sun, L. First-principle calculations of lithium adsorption and diffusion on titanium-based monolayers. *Chem. Phys.* **2020**, *539*, No. 110956.
(55) Yekta, Y.; Hadipour, H.; Şaşıoğlu, E.; Friedrich, C.; Jafari, S. A.; Blügel, S.; Mertig, I. Strength of effective Coulomb interaction in two-dimensional transition-metal halides MX_2 and MX_3 (M = *Ti, V, Cr, Mn, Fe, Co, Ni*; X = *Cl, Br, I*). *Phys. Rev. Mater.* **2021**, *5*, No. 034001.
(56) Wu, S.; Li, A.; Yang, Z.; Ouyang, F. Electronic structures and magnetic properties of 3d transition metal doped monolayer RhI_3. *Chem. Phys. Lett.* **2022**, *799*, No. 139643.
(57) Zhang, P.; Yuan, J.-H.; Fang, W.-Y.; Li, G.; Wang, J. Two-dimensional V-shaped PdI_2: Auxetic semiconductor with ultralow lattice thermal conductivity and ultrafast alkali ion mobility. *Appl. Surf. Sci.* **2022**, *601*, No. 154176.
(58) Li, B.; Yang, Y.; Sun, Z.; Qi, H.; Xiong, Z.; Wu, K.; Li, H.; Sun, K.; Xiao, X.; Shen, C.; Wang, N. First-Principles Investigation on the Significant Anisotropic Thermoelectric Transport Performance of a Hf_2Cl_4 Monolayer. *J. Phys. Chem. C* **2022**, *126*, 525−533.
(59) Tang, H.; Huang, Y.; Yuan, H.; Chen, H. Layered $TiCl_2$ Monolayer as an Antiferromagnetic Semiconductor. *SPIN* **2022**, *12*, No. 2250004.
(60) Cao, T.; Wang, G.; Han, W.; Ye, H.; Zhu, C.; Shi, J.; Niu, Q.; Tan, P.; Wang, E.; Liu, B.; Feng, J. Valley-Selective Circular Dichroism of Monolayer Molybdenum Disulphide. *Nat. Commun.* **2012**, *3*, No. 887.
(61) Wang, X.; Qi, H.; Wang, N.; Wang, Z.; Tang, W.; Tan, Z.; Zhu, Z.; Zhang, M.; Shen, C. Unexpectedly high thermoelectric performance of anisotropic Zr_2Cl_4 monolayer. *J. Phys.: Condens. Matter* **2023**, *35*, No. 394001.
(62) Chen, W.; Pasquarello, A. Band-Edge Levels in Semiconductors and Insulators: Hybrid Density Functional Theory versus Many-Body Perturbation Theory. *Phys. Rev. B* **2012**, *86*, No. 035134.
(63) Patra, A.; Jana, S.; Samal, P.; Tran, F.; Kalantari, L.; Doumont, J.; Blaha, P. Efficient Band Structure Calculation of Two-Dimensional Materials from Semilocal Density Functionals. *J. Phys. Chem. C* **2021**, *125*, 11206−11215.
(64) Park, S.; Mutz, N.; Schultz, T.; Blumstengel, S.; Han, A.; Aljarb, A.; Li, L.-J.; List-Kratochvil, E. J. W.; Amsalem, P.; Koch, N. Direct Determination of Monolayer MoS_2 and WSe_2 Exciton Binding Energies on Insulating and Metallic Substrates. *2D Mater.* **2018**, *5*, No. 025003.
(65) Zhang, G.; Chaves, A.; Huang, S.; Wang, F.; Xing, Q.; Low, T.; Yan, H. Determination of Layer-Dependent Exciton Binding Energies in Few-Layer Black Phosphorus. *Sci. Adv.* **2018**, *4*, No. eaap9977.
(66) Qiao, M.; Liu, J.; Wang, Y.; Li, Y.; Chen, Z. PdSeO3 Monolayer: Promising Inorganic 2D Photocatalyst for Direct Overall Water Splitting Without Using Sacrificial Reagents and Cocatalysts. *J. Am. Chem. Soc.* **2018**, *140*, 12256−12262.
(67) Kwak, J. Y. Absorption Coefficient Estimation of Thin MoS_2 Film Using Attenuation of Silicon Substrate Raman Signal. *Results Phys.* **2019**, *13*, No. 102202.
(68) Anderson, R. L. Germanium-Gallium Arsenide Heterojunctions [Letter to the Editor]. *IBM J. Res. Dev.* **1960**, *4*, 283−287.
(69) Molina-Sánchez, A.; Palummo, M.; Marini, A.; Wirtz, L. Temperature-Dependent Excitonic Effects in the Optical Properties of Single-Layer MoS_2. *Phys. Rev. B* **2016**, *93*, No. 155435.
(70) Zhu, B.; Chen, X.; Cui, X. Exciton Binding Energy of Monolayer WS_2. *Sci. Rep.* **2015**, *5*, No. 9218.

https://doi.org/10.1021/acsaem.5c00610
ACS Appl. Energy Mater. XXXX, XXX, XXX−XXX